Technical University of Denmark

DTU

Magnetic characterization of synthetic titanomagnetites: Quantifying the recording fidelity of ideal synthetic analogs

Almeida, Trevor P.; Muxworthy, Adrian R.; Williams, Wyn; Kasama, Takeshi; Dunin-Borkowski, Rafal E.

DTU Library
Technical Information Center of Denmark

Geochemistry Geophysics Geosystems G^3

Magnetic characterization of synthetic titanomagnetites: Quantifying the recording fidelity of ideal synthetic analogs

Trevor P. Almeida and Adrian R. Muxworthy

Department of Earth Science and Engineering, Imperial College London, South Kensington Campus, London SW7 2AZ, UK (t.almeida@imperial.ac.uk)

Wyn Williams

School of GeoSciences, University of Edinburgh, King's Buildings, Edinburgh, UK

Takeshi Kasama

Centre for Electron Nanoscopy, Technical University of Denmark, Kongens Lyngby, Denmark

Rafal Dunin-Borkowski

Ernst Ruska-Centre for Microscopy and Spectroscopy with Electrons and Peter Grünberg Institute, Forschungszentrum Jülich, Jülich, Germany

[1] A series of four synthetic basalts comprising titanomagnetite ($Fe_{3-x}Ti_xO_4$) grains of varied size and titanium content have been produced by a glass-ceramic method. Complementary characterization techniques of X-ray diffractometry, secondary electron microscopy, and transmission electron microscopy (TEM) demonstrate the reaction product composition consisted of mainly $Fe_{3-x}Ti_xO_4$, pyroxene hedenbergite, fayalite, and SiO_2. The samples exhibit bimodal distributions of larger (<2 μm) and smaller $Fe_{3-x}Ti_xO_4$ particles (<50 nm in diameter), the latter found inside pyroxene crystals, as well as the sporadic occurance of dendritic $Fe_{3-x}Ti_xO_4$ structures. Magnetic measurements show their bulk characteristics fall into two groups: Ti-rich titanomagnetite samples with varying Ti content; and near-stoichiometric magnetite. The TEM technique of off-axis electron holography allowed for visualization of the magnetic behavior of the synthetic $Fe_{3-x}Ti_xO_4$ grains. Energy dispersive X-ray analysis and off-axis electron holography confirmed the small $Fe_{3-x}Ti_xO_4$ grains (<50 nm) confined within glassy pyroxene regions to be Fe-rich and single domain, carrying strong magnetic signals, compared to the relatively magnetically weak larger $Fe_{3-x}Ti_xO_4$ grains ($x \sim 0.6$). The large grains in the pure magnetite sample are shown to be pseudo-single domain in nature. The quenching process involved in synthesis is considered similar to that of pillow basalts found at mid-ocean ridges and hence the reaction products are thought ideal in terms of characterization and understanding, for the purpose of studying natural systems.

1. Introduction

[2] Our knowledge of the geomagnetic field's variance on geological timescales is dependent on our ability to recover meaningful palaeomagnetic signals from rocks and sediments. Hence, it is important to understand the formation and recording mechanisms, as well as fidelity, of the magnetic minerals within natural systems. The most common magnetic minerals on Earth, and the main recorders in igneous rocks including mid-ocean ridge basalts (MORB), fall within the iron-titanium-oxide system [*Dunlop and Özdemir*, 1997] and generally provides the only recoverable absolute palaeointensities (as well as palaeo-directions). Such full vector data is essential to fully reconstruct the ancient geomagnetic field behavior.

[3] Although the iron-titanium-oxide system has been widely studied over the years, there are still gaps in our knowledge. Most previous studies have looked at natural systems [e.g., *Bleil and Petersen*, 1983; *Krása et al.*, 2005], with only a few investigations focusing on synthetic samples where the magnetic minerals formation history is tightly constrained [e.g., *Özdemir and Banerjee*, 1981; *Halgedahl*, 1991; *Zitzelsberger and Schmidbauer*, 1996]. Key questions still remain as to the formation of Ti-rich iron oxide minerals in the common single domain (SD) to pseudo-single domain (PSD) grain-size range: (1) what are the micromagnetic structures within Ti-rich iron oxide PSD grains, how do these affect their recording fidelity and (2) what is the variation in stoichiometry of the particles. Evidence suggests there is a stoichiometric variance with grain size [*Zhou et al.*, 1997, 2000] which will give rise to misleading Curie temperatures if determined by an in-field thermomagnetic measurement (an M_s-T curve, where M_s is the saturation magnetization and T is the temperature), i.e., the smallest grains carrying the remanence will have a different stoichiometry to the larger grains that dominate the M_s-T curve.

[4] In this paper, a microscopic and magnetic study of a suite of iron-titanium-oxides synthesized in the laboratory using the glass-ceramic method developed by *Worm and Markett* [1987], is reported. This technique has been refined to gain a better control of the grain size and spatial distribution, allowing the synthesis of Ti-rich iron oxides in the SD to PSD grain size range. The transmission electron microscopy (TEM) technique of off-axis electron-holography [*Dunin-Borkowski et al.*, 1998; *Harrison et al.*, 2002; *Kasama et al.*, 2013] has been applied to synthetic Ti-rich PSD iron oxides for the first time, and an investigation of the behavior of SD and PSD grains as a function of temperature is presented.

2. Methods and Experimental Procedures

[5] Synthetic basalts containing $Fe_{3-x}Ti_xO_4$ were prepared by a glass-ceramic method, as described previously [*Worm and Markert*, 1987]. Samples were synthesized from laboratory grade powders of Fe_2O_3, SiO_2, TiO_3, $CaCO_3$, K_2CO_3, and Na_2CO_3, as summarized in Table 1. The powders were mixed in acetone using a pestle and mortar and once dry combined with aqueous polyethylene oxide solution to form a viscous slurry and pressed into pellets ($\sim$5 mm in diameter) on the end of Pt wires. The pellets were suspended in a vertical temperature controlled tube furnace under an oxygen partial pressure provided by a CO-CO$_2$ gas flow of ratio 1:10. The sample was melted at 1400°C for 15 h to equilibrate Fe^{2+}/Fe^{3+} ratios with the oxygen fugacity. The Pt wires were then released and the molten pellets subsequently quenched in the bottom of the tube furnace. After quenching the pellets were reheated at 750°C for 3 h using the same method, and quenched again.

[6] For the purpose of structural characterization, quenched pellets were crushed into a fine powder using the pestle and mortar, dispersed on a Si substrate and examined using X-ray diffractometry (XRD) (PANalytical X'Pert PRO Diffractometer). Additional pellets were mounted in epoxy resin and polished for the purpose of survey secondary electron microscopy (SEM) (FEI Quanta 200 ESEM FEG), whilst their elemental constituents

Table 1. Summary of Precursor Powders Blended into Synthetic Melt Compositions

	Sample S1		Sample S2		Sample S3		Sample S4	
Precursor	Mass (g)	Melt (%)	Mass (g)	Melt (%)	Mass (g)	Melt (%)	Mass (g)	Melt (%)
SiO_2	0.287	28.7	0.287	30.1	0.431	34.8	0.287	31.4
$CaCO_3$	0.155	15.5	0.155	16.2	0.233	18.8	0.155	17.0
Na_2CO_3	0.061	6.1	0.061	6.4	0.092	7.4	0.061	6.7
K_2CO_3	0.061	6.1	0.061	6.4	0.092	7.4	0.061	6.7
Fe_2O_3	0.349	34.9	0.348	36.4	0.348	28.1	0.348	38.2
TiO_2	0.087	8.7	0.043	4.5	0.044	3.5	0	0
Total	*1*	*100*	*0.955*	*100*	*1.240*	*100*	*0.912*	*100*

were identified using energy despersive X-ray analysis (EDX) (Aztec, Oxford Instruments). Desirable regions of the polished samples were isolated, ion-milled into lamallae and lifted out using a focused ion beam (FIB) and Omniprobe system (Helios NanoLab 600) for localized examination using TEM. Conventional bright field (BF) imaging was performed using a FEI Tecnai TEM operated at 200 kV (Centre for Electron Nanoscopy (CEN), Technical University of Denmark), with EDX analysis (Aztec, Oxford Instruments) and selected area electron diffraction (SAED) allowing for chemical and phase identification, respectively. For the purpose of electron holography, a FEI Titan with a C_S corrector on the condenser lens, equipped with a Lorentz lens and biprism, was used at 300 kV (CEN). Off-axis electron holograms were recorded in Lorentz mode with the objective lens switched off and the specimen in magnetic-field-free conditions at room temperature. Mean inner potential contributions to the recorded phase shift were removed by using in situ magnetization reversal [*Kasama et al.*, 2011].

[7] The magnetic measurements were conducted at the palaeomagnetic laboratory at Imperial College London and the Institute for Rock Magnetism (I.R.M), University of Minnesota. High-temperature thermomagnetic curves were measured using a Princeton Measurements Vibrating Sample Magnetometer (VSM) fitted with a furnace; heating was performed in flowing He. Low-temperature hysteresis measurements were made from 15 to 295 K (in 10 K intervals) using a Princeton Measurements VSM. A Quantum Designs Magnetic Properties Measuring Systems (MPMS) cryogenic magnetometer was used to measure cooling and warming curves of room temperature (RT) induced saturation isothermal remanence magnetization (SIRM) to identify low-temperature crystallographic transitions, as well as warming curves of SIRM at 10 K after field cooling (FC) at 2.5 T and zero-field cooling (ZFC), from 300 K to 10 K.
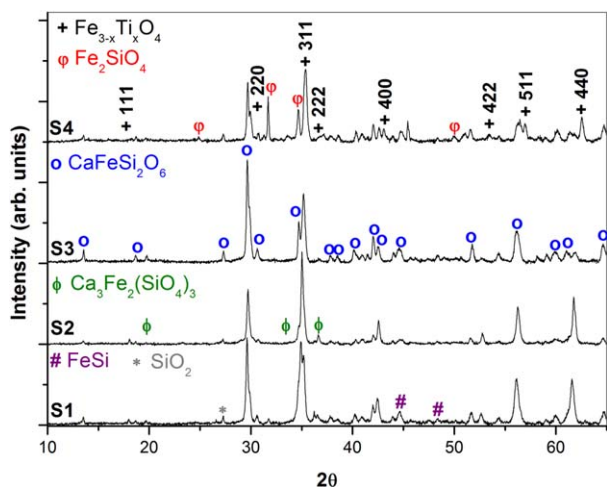
3. Results

3.1 X-Ray Diffraction analysis

[8] The XRD patterns of Figure 1 provide information on the crystal structure of both the synthesized $Fe_{3-x}Ti_xO_4$ particles and supporting glass-ceramic matrix. The peaks in Samples S1–S4 are in good agreement with the presence of $Fe_{3-x}Ti_xO_4$, and characteristic to the phases Fe_2TiO_4 (Joint Committee on Powder Diffraction standards (JCPDS) reference 72-1665), $Fe_{2.5}Ti_{0.5}O_4$ (JCPDS 75-1376), and Fe_3O_4 (JCPDS 88-0315). In addition, all XRD patterns display peaks characteristic to the pyroxene hedenbergite ($CaFeSi_2O_6$, JCPDS 70-1876), andradite ($Ca_3Fe_2(SiO_4)_3$, JCPDS 84-1938), FeSi (JCPDS 86-0795), SiO_2 (JCPDS 83-0540), and Fayalite (Fe_2SiO_4,

Figure 1. XRD patterns of Samples S1–S4 confirming the presence of $Fe_{3-x}Ti_xO_4$, indexed to $Fe_{2.5}Ti_{0.5}O_4$ (JCPDS 75-1376), as well as the additional phases of $CaFeSi_2O_6$, $Ca_3Fe_2(SiO_4)_6$, FeSi, and SiO_2.
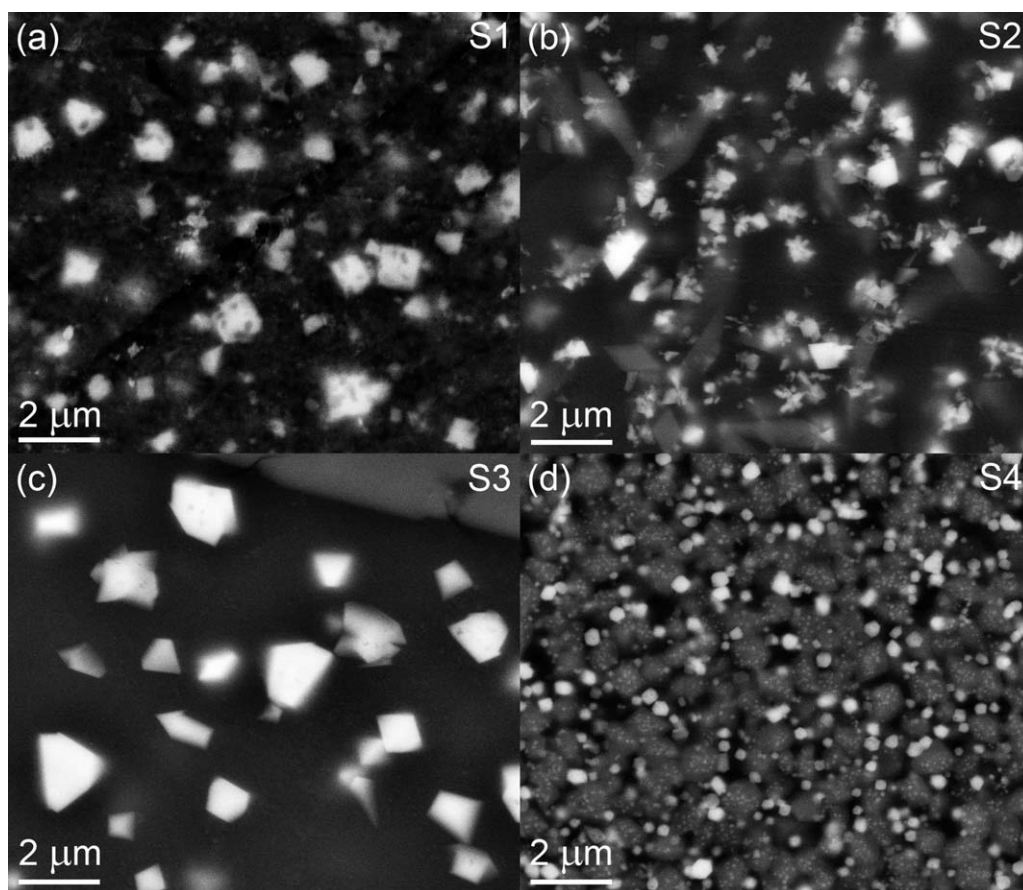
Figure 2. (a–d) BSE SEM images of Samples S1–S4, where $Fe_{3-x}Ti_xO_4$ particles (bright regions) are dispersed within the glass-ceramic matrix.

JCPDS 71-1673), with the latter more dominant in Sample S4.

3.2. Scanning-Electron Microscopy Imaging and Analysis

[9] The backscattered-electron (BSE) SEM images (Figure 2) provide information on the size and morphology of the $Fe_{3-x}Ti_xO_4$ particles dispersed in the glass ceramic matrix. In samples S1 and S2 (Figures 2a and 2b respectively), the $Fe_{3-x}Ti_xO_4$ particles (bright regions) are generally isotropic and $<\sim1.6$ μm in size, with clusters of smaller $Fe_{3-x}Ti_xO_4$ particles in the latter. Figure 2c shows sample S3 to comprise slightly larger $Fe_{3-x}Ti_xO_4$ particles ($<\sim2.8$ μm), whilst sample S4 is observed to consist of markedly smaller $Fe_{3-x}Ti_xO_4$ particles ($<\sim0.7$ μm, Figure 3d). Allocation of an appropriate gray value threshold for the BSE SEM images allowed for creation of binary contrast images, with the extrapolated particle-size

distribution and nearest-neighbor distance data of samples S1–S4 summarized in Figure 3 [*Beggan and Hamilton*, 2010]. However, the particle size analysis is limited by the resolution of the SEM and resulting pixel size, with sizes below <100 nm considered unreliable for the magnification of the acquired images.

[10] The BSE SEM and corresponding EDX compositional maps (Figure 4) present the elemental distribution within sample S1. Comparison of the BSE image (Figure 4a) with the Fe and Ti compositional maps (Figures 4b and 4c) confirm the bright regions in the BSE image are rich in Fe and Ti, and hence attributed as $Fe_{3-x}Ti_xO_4$ particles. The remaining area is shown to be rich in Si (Figure 4d) and assigned as the glass silicon matrix, which exhibits areas high in Ca content (Figure 4e), considered as hedenbergite phase regions. Figure 4f shows the oxygen content to be uniformly distributed across the sample.
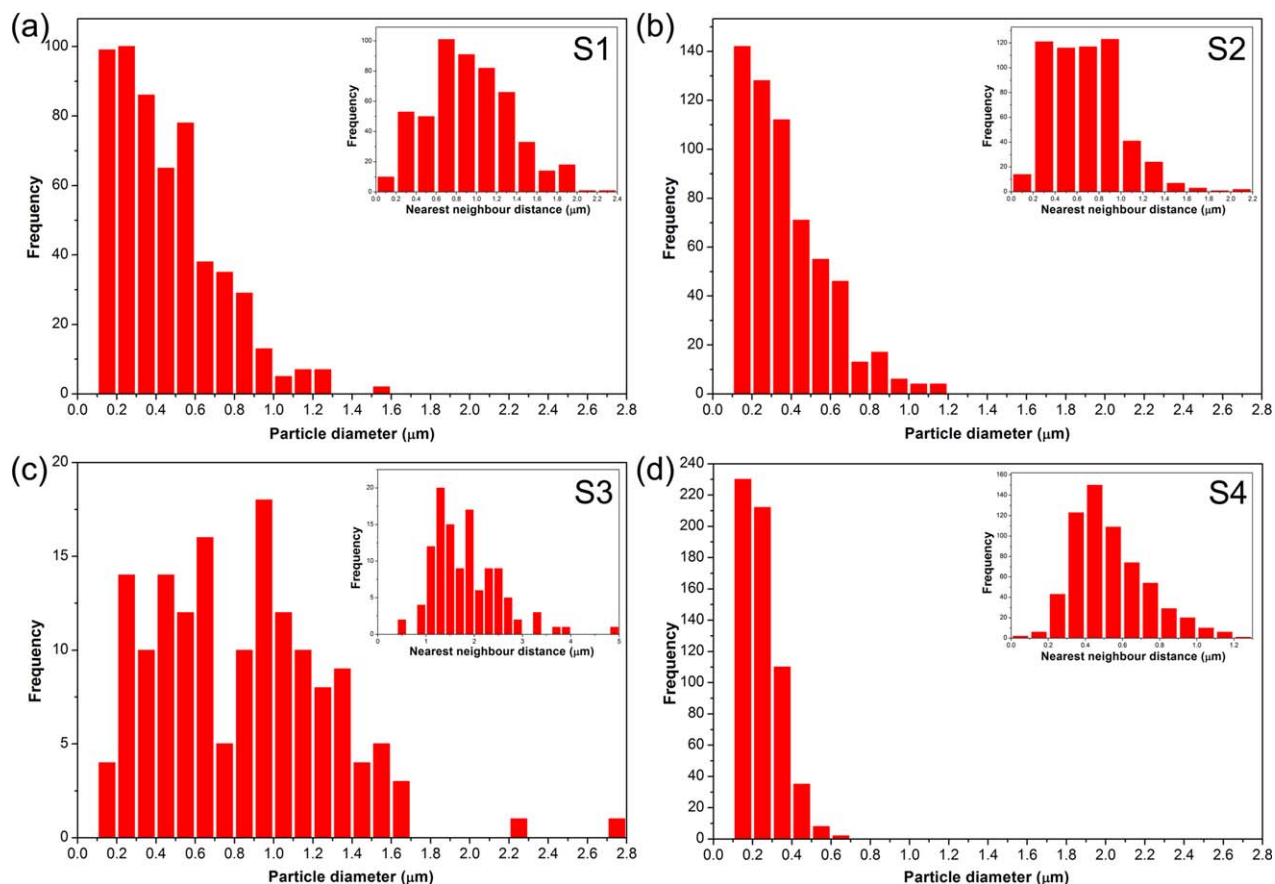
Figure 3. (a–d) Particle size distributions of Samples S1–S4, along with nearest neighbor distance (inset).

3.3. Transmission Electron Microscopy Imaging and Analysis

[11] The BF TEM images of Figure 5 provide a closer examination of the $Fe_{3-x}Ti_xO_4$ particles and surrounding glass ceramic matrix. Figure 5a reveals the various sizes of the $Fe_{3-x}Ti_xO_4$ grains in Sample S1, as confirmed by SAED (Figure 5a, inset, indexed to $Fe_{2.5}Ti_{0.5}O_4$ (JCPDS 75-1376)). A large single crystal $Fe_{3-x}Ti_xO_4$ grain in the PSD region ($\sim$500 nm) is presented in Figure 5b, as confirmed by SAED (Figure 5b, inset). Figure 5c shows a much smaller $Fe_{3-x}Ti_xO_4$ grain, surrounded by the Ca-rich hedenbergite phase, as identified by characteristic lattice fringes corresponding to {220} planes (Figure 5c, inset). The associated EDX spectra of Figure 5d, acquired from the $Fe_{3-x}Ti_xO_4$ grains presented in Figures 5b and 5c, show a markedly weaker Ti signal acquired from the smaller $Fe_{3-x}Ti_xO_4$ grain (Figure 5c). The BF TEM image of Sample S4 (Figure 5e) displays large $Fe_{3-x}Ti_xO_4$ grains ($\sim$500 nm), distinct from smaller $Fe_{3-x}Ti_xO_4$ grains ($\sim$100 nm) which appear to be concentrated in the Ca-rich glassy hedenbergite regions of the matrix, as identified in the SEM data. Examples of the larger $Fe_{3-x}Ti_xO_4$ grains ($\sim$300 nm) in Sample S4 are shown in Figure 5f.

[12] Figure 6a presents a high angle annular dark field (HAADF) image of Sample S4, showing larger Fe_3O_4 grains and Ca-rich glassy regions confining smaller Fe_3O_4 grains ($<$50 nm). The EDX maps of Figures 6b–6d acquired from the boxed region in Figure 6a depicts the (b) Fe, (c) Si, and (d) Ca content. The bottom right corner of the boxed region (arrowed in Figures 6a, 6b, and 6d) of the matrix is absent of both Fe and Ca, further suggesting the glassy regions within the SiO_2 matrix are $CaFeSi_2O_6$ or $Ca_3Fe_2(SiO_4)_3$, whilst the smaller Fe-rich Fe_3O_4 grains are clear to see. The SEM and TEM images of samples S1 (Figure 7a) and S4 (Figure 7b), respectively, display the dendritic structures found sporadicly across these synthetic basalts. Dendritic structures are normally associated with rapid quenching [*Dantzig and Rappaz*, 2009].
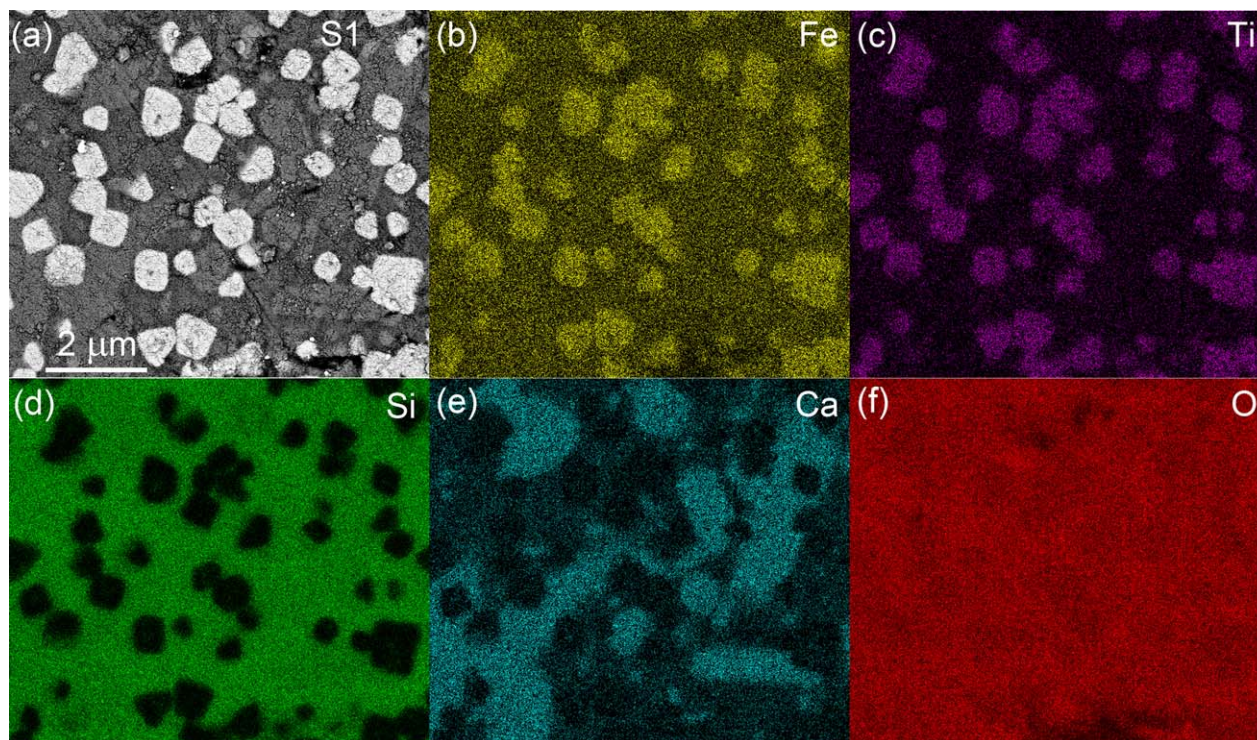
Figure 4. (a) BSE SEM image of Sample S1 showing $Fe_{3-x}Ti_xO_4$ particles dispersed within the glass-ceramic matrix and EDX compositional maps displaying its (b) iron; (c) titanium; (d) silicon; (e) calcium and (f) oxygen, content.

[13] The off-axis electron holography presented in Figures 8–10 allowed for the imaging of the in-plane magnetization of Samples S1 and S4, respectively. Figure 8a shows an electron hologram of sample S1 comprising several larger $Fe_{3-x}Ti_xO_4$ grains (labeled a) and two smaller $Fe_{3-x}Ti_xO_4$ particles (∼50 nm, labeled b). The magnetic induction map of Figure 8b depicts the magnetic field contours to be concentrated to the smaller $Fe_{3-x}Ti_xO_4$ particles (magnified in Figure 8c), where the magnetic field direction is imaged as downward (Figure 8d) through SD $Fe_{3-x}Ti_xO_4$ grains. Figure 9a presents an electron hologram of an individual $Fe_{3-x}Ti_xO_4$ grain (∼350 nm) in Sample S4, where the corresponding magnetic induction map shows a magnetic vortex (Figure 9b). The electron hologram of Figure 10a displays an individual $Fe_{3-x}Ti_xO_4$ grain (∼220 nm), again in sample S4, where the corresponding magnetic induction map (Figure 10b) shows its PSD (vortex) nature, which contains both a magnetic vortex and a stray magnetic field similar to that expected for a SD particle.

3.4. Magnetic Measurements

[14] High-temperature thermomagnetic analysis indicated that the samples were thermally stable (Figure 11). Curie temperatures were determined using the second-derivative method [*Tauxe*, 1998] (Table 2). Samples S1 and S3 yielded two distinct Curie temperatures: S1, 83°C and 569°C; and S3, 119°C and 579°C; whereas sample S2 had a broad Curie temperature range, 382–432°C, and a Curie temperature at 579°C; whilst sample S4 exhibited a single Curie temperature of 579°C. The higher Curie temperatures are indicative of near-stoichiometric magnetite, whereas the lower Curie temperatures suggest the presence of the second phase, with significant Ti content.

[15] Measurement of the following room-temperature hysteresis parameters are summarized in Table 2: the remanent saturation magnetization M_{rs}; saturation magnetization M_s; coercivity of remanence B_{cr}; and coercivity B_c. All four samples display hysteresis parameters that are traditionally indicative of PSD hysteresis behavior. It is observed that all samples are plotted within the PSD region, however, sample S1 has a high M_{rs}/M_s raio, which is indicative of SD-like behavior, whilst sample S4 displays the least SD-like characteristics.

[16] First-order reversal curve (FORC) diagrams [*Roberts et al.*, 2000] were measured for the four
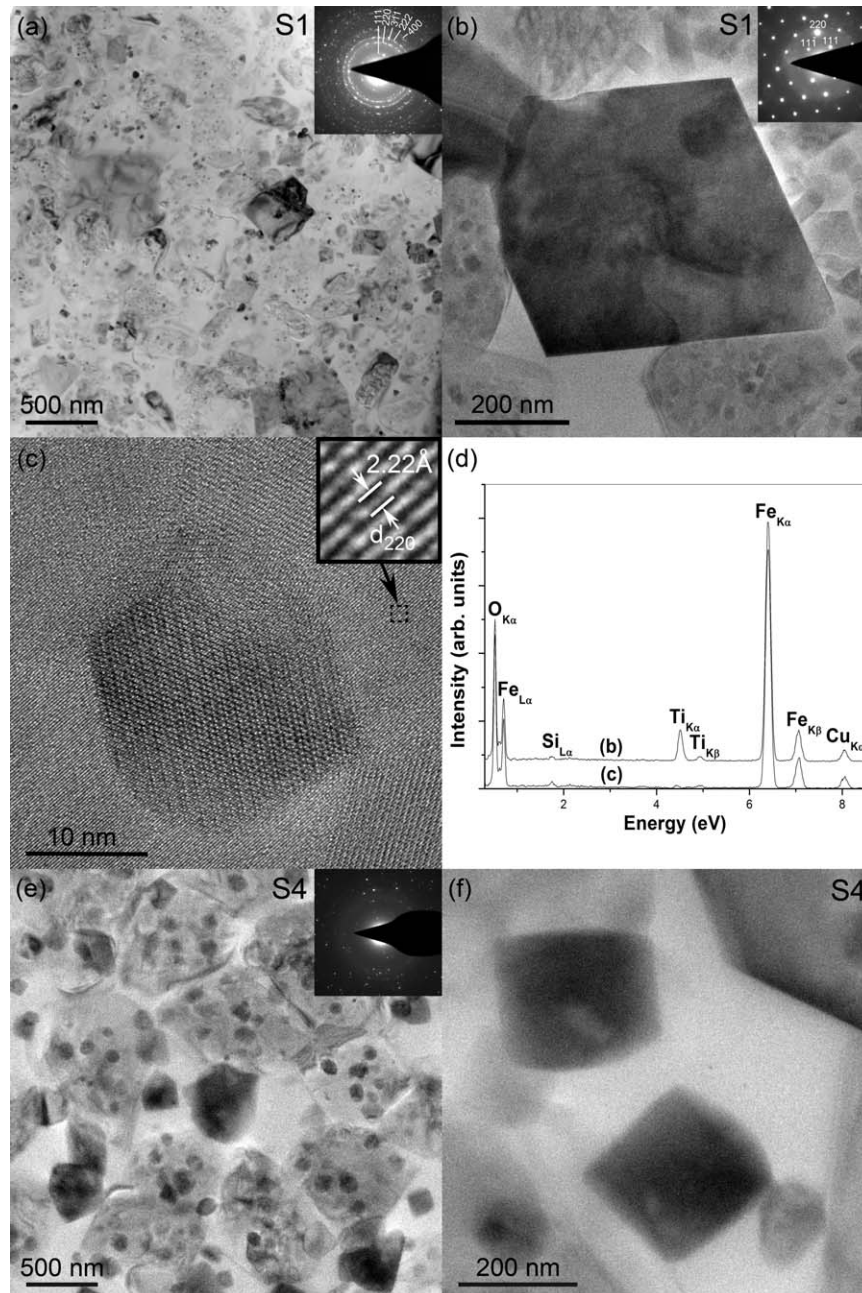
Figure 5. BF TEM images of (a) $Fe_{3-x}Ti_xO_4$ grains (Sample S1) of various sizes dispersed within a glass matrix and SAED (inset, indexed to $Fe_{2.5}Ti_{0.5}O_4$ (JCPDS 75–1376); (b) an individual single crystal $Fe_{3-x}Ti_xO_4$ grain (Sample S1) in the PSD size range (∼500 nm) and SAED (inset, indexed); (c) small $Fe_{3-x}Ti_xO_4$ grain confined in hedenbergite glassy region, as identified by characteristic lattice fringes (inset). (d) Associated EDX spectra acquired from the $Fe_{3-x}Ti_xO_4$ grains shown in Figures 5b and 5c. BF diffraction contrast TEM images of (e) large (∼500 nm) and small $Fe_{3-x}Ti_xO_4$ grains (∼100 nm) (Sample S4), with the latter concentrated in the hedenbergite glassy regions of the matrix; and (f) examples of the larger $Fe_{3-x}Ti_xO_4$ grains (∼300 nm) in Sample S4.

samples (Figure 12). All the samples displayed PSD/SD type behavior with distinct peaks [*Muxworthy and Dunlop*, 2002]. The FORC distribution of Sample S3 is markedly different from the other three, with extension along the B_c axis. Samples S2 and S3 display FORC distributions that slope slightly toward lower B_u values as B_c increases; this is indicative of negative mean-interaction
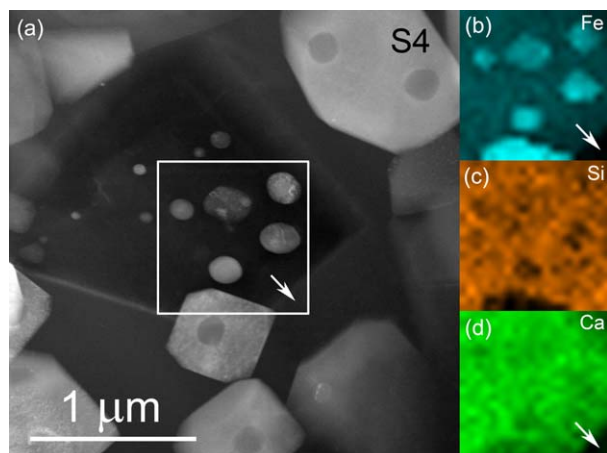
Figure 6. (a) HAADF image of Sample S4 showing larger Fe_3O_4 grains and Ca-rich glassy regions confining smaller Fe_3O_4 grains (<150 nm). (b–d) EDX maps acquired from the boxed region in Figure 6a showing the (b) Fe, (c) Si, and (d) Ca content.

fields [*Pike et al.*, 1999]. The near-stoichiometric magnetite sample S4 exhibited behavior characteristic of ideal single-domain grains, however, no negative region close to the vertical B_u-axis is observed, indicating that the controlling anisotropy is not uniaxial, but likely a mixture of cubic and unixial anisotropy [*Muxworthy et al.*, 2004; *Newell*, 2005].

[17] Low-temperature SIRM warming curves (Figure 13) display a range of behaviors. In all four samples, the sharp drop in the remanence on initial cooling is indicative of very small nanometric grains, which are superparamagnetic at room temperature. Sample S4 (Figure 13d), displays behavior typical of near stoichiometric magnetite with a

Verwey transition of ~120 K. The large drop in the remanence at the Verwey transition suggests that the magnetic remanence is dominated by the magnetocrystalline anisotropy. Samples S1, S2, and S3 all display kinks in their SIRM warming curves ~50–80 K, which is indicative of $x = 0.4$–0.6 in $Fe_{3-x}Ti_xO_4$ [*Moskowitz et al.*, 1998], though the relatively small drops in magnetization compared to *Moskowitz et al.* [1998] is attributed to the smaller mean grain size of the samples in this study. Sample S1 also displays a kink in the FC warming curve at ~270 K, which is not seen in the ZFC curve and hence likely due to unblocking of SD grains.

[18] Low-temperature cycling of the SIRM to 10 K (Figure 14), reveals different trends: samples S1 and S2 both demagnetize on cooling without displaying a sharp Verwey transition, sample S4 displays similar behavior, though the Verwey transition is more clearly defined, whilst sample S3 does not display significant demagnetization during cooling; its behavior is almost reversible. The behavior of samples S1 and S2 is typical of titanomagnetite with a low Ti-content with a PSD domain state [*Özdemir and Dunlop*, 2003], whilst sample S4 is indicative of near-stoichiometric PSD magnetite [*Muxworthy and McClelland*, 2000]. In contrast, the behavior of S3 is typical for Ti-rich or SD titanomagnetite [*Muxworthy and McClelland*, 2000].

[19] The hysteresis parameters B_c and M_{rs}/M_s are plotted as a function of temperature (15 K to 295 K) in Figure 15. Sample S4 displays behavior for both B_c and M_{rs}/M_s typical of PSD/MD magnetite [*Muxworthy*, 1999], e.g., on warming B_c drops
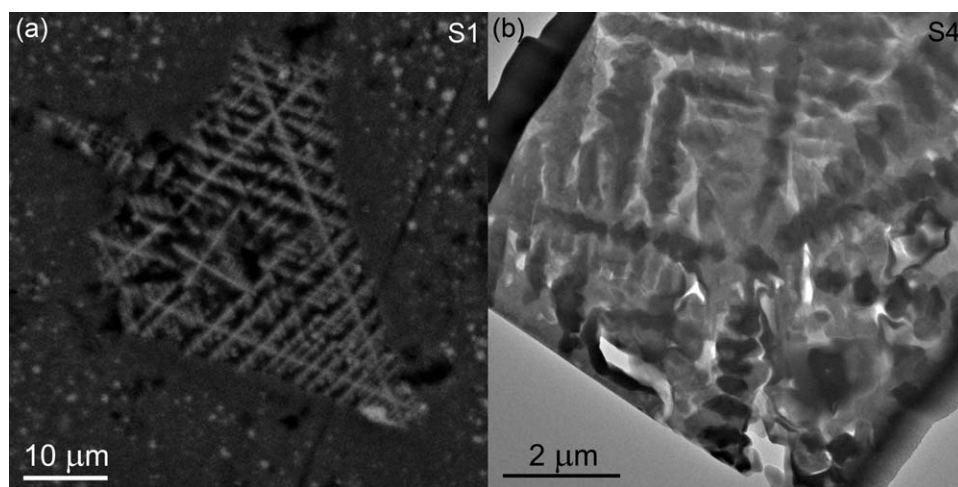

Figure 7. (a) SEM and (b) TEM images of dendritic structures found in samples S1 and S4, respectively.
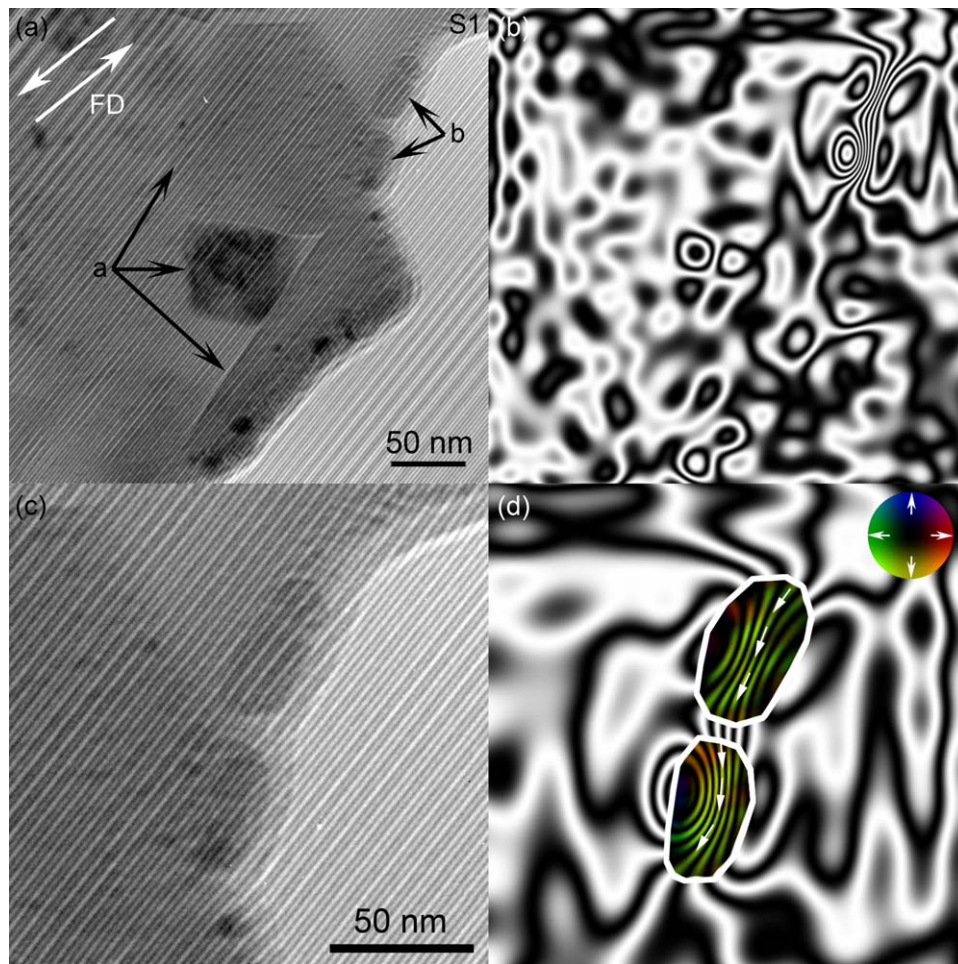
Figure 8. (a) Electron hologram of Sample S1 comprising several larger $Fe_{3-x}Ti_xO_4$ grains (labeled a) and two smaller $Fe_{3-x}Ti_xO_4$ particles ($\sim$50 nm, labeled b), with the arrows showing direction of the applied saturating field. (b) Corresponding magnetic induction map recorded at remanence after saturating the elements upwards, showing magnetic field contours concentrated to the two smaller $Fe_{3-x}Ti_xO_4$ grains. (c) Magnification of the two smaller $Fe_{3-x}Ti_xO_4$ particles (labeled b in Figure 8a). (d) Corresponding magnetic induction map recorded at remanence and arrows show the local magnetization directions. The contour spacing is 0.098 radians and magnetization direction is depicted in the color wheel (inset).

sharply between 100 and 120 K, before increasing as the temperature increases to the room temperature. In contrast, samples S1–S3 display a general decrease in B_c and M_{rs}/M_s on warming from 15 K to 295 K with no pronounced change in behavior around the Verwey transiton, which is typical of Ti-rich titanomagnetite [*Hodych and Matzka*, 2004].

4. Discussion

[20] All four samples were formed by quenching, making their formation history more similar to the pillow basalts found at mid-ocean ridges than the slowly cooled subaerial basalts found elsewhere. The effect of rapid cooling is clearly seen by the presence of dentritic structures (Figure 7) [*Shaar and Feinberg*, 2013]. In all the samples there appear to be bimodal distributions of particles: larger particles which are readily observed under the SEM data (Figure 2), and smaller particles (<50 nm in diameter), which are found inside pyroxene crystals (Figure 6). These smaller crystals are only seen under the TEM in this instance. It is believed this is the first report of magnetic inclusions within the synthetic pyroxene "single-crystals" [*Tarduno and Cottrell*, 2005]. Such magnetic inclusions are thought to be ideal recorders of the ancient magnetic field, as they are both
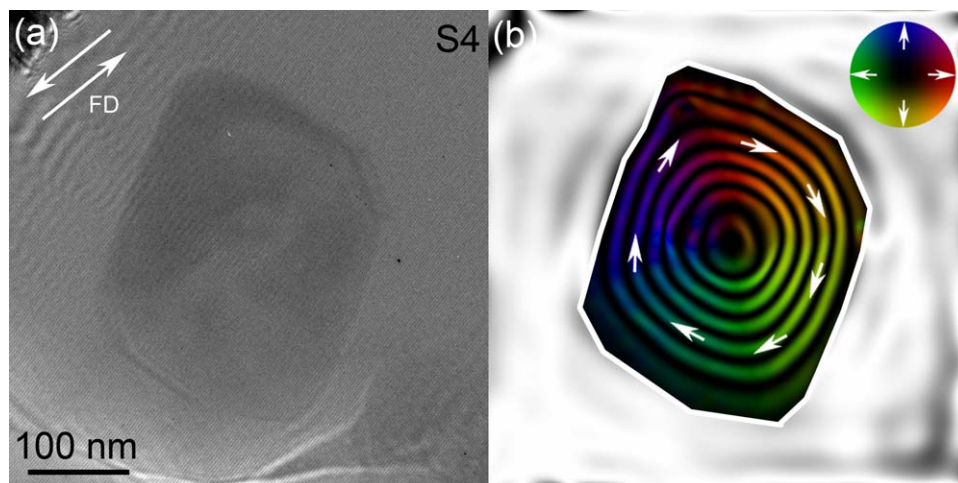
Geochemistry
Geophysics
Geosystems

G^3

ALMEIDA ET AL.: MAGNETISM OF SYNTHETIC TITANOMAGNETITES

10.1002/2013GC005047

Figure 9. (a) Electron hologram of an individual $Fe_{3-x}Ti_xO_4$ grain ($\sim$220 nm) in Sample S4 and (b) its corresponding magnetic induction map, showing a magnetic vortex. The contour spacing is 2.09 radians and magnetization direction is depicted in the color wheel (inset).

small, and enclosed and protected from weathering. That these grains can be easily grown in the laboratory is encouraging, and shows that such "single-crystals" are not unique, but likely ubiquitous, i.e., the scope for recovering and studying such crystals is high. The larger crystals, which are thought to contain more titanium, display PSD vortex structures similar to those reported for stoichiometric PSD magnetite. In these still relatively small particles, the effects of magnetostriction are not so readily observed in the domain patterns when compared to larger Ti-rich iron oxides [*Moskowitz et al.*, 1988]. This implies that the magnetic remanence carried by PSD titanomagnetite crystals is not so strongly effected by local stress variations and is a better recorders of the geomagnetic field than the remanence of larger Ti-rich iron-oxide grains.

[21] The bulk characteristics and behavior of the four samples fall into two groups: samples S1, S2, and S3, and sample S4. Samples S1, S2, and S3 are Ti-rich titanomagnetite samples with varying Ti content, whilst sample S4 is indicative of near-stoichiometric magnetite; however, within the titanomagnetite rich samples, there is variability that is not consistent, e.g., S2 and S3 display similar magnetic hystereis parameters (Table 2), though
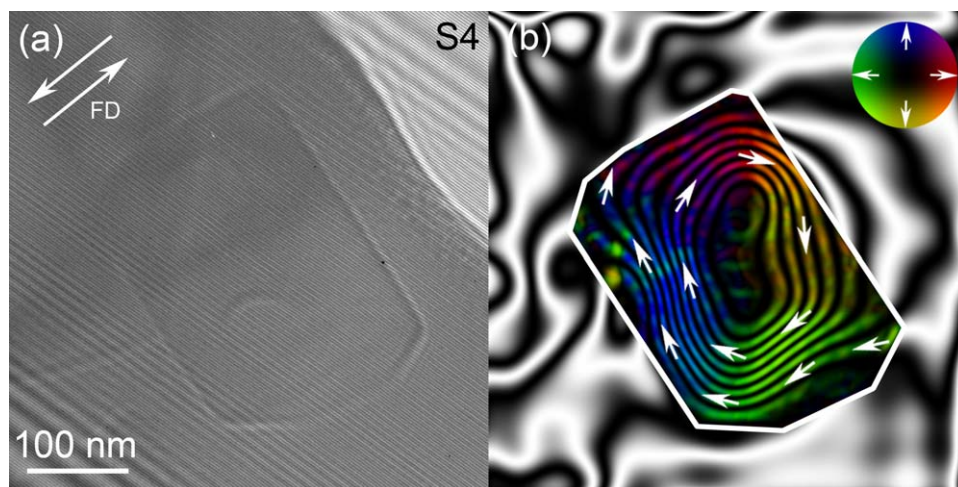

Figure 10. (a) Electron hologram of an individual $Fe_{3-x}Ti_xO_4$ grain ($\sim$220 nm) in Sample S4 and (b) revealing the PSD nature of the particle, which contains both a magnetic vortex and a stray magnetic field similar to that expected for a SD particle. The contour spacing is 0.52 radians and magnetization direction is depicted in the color wheel (inset).
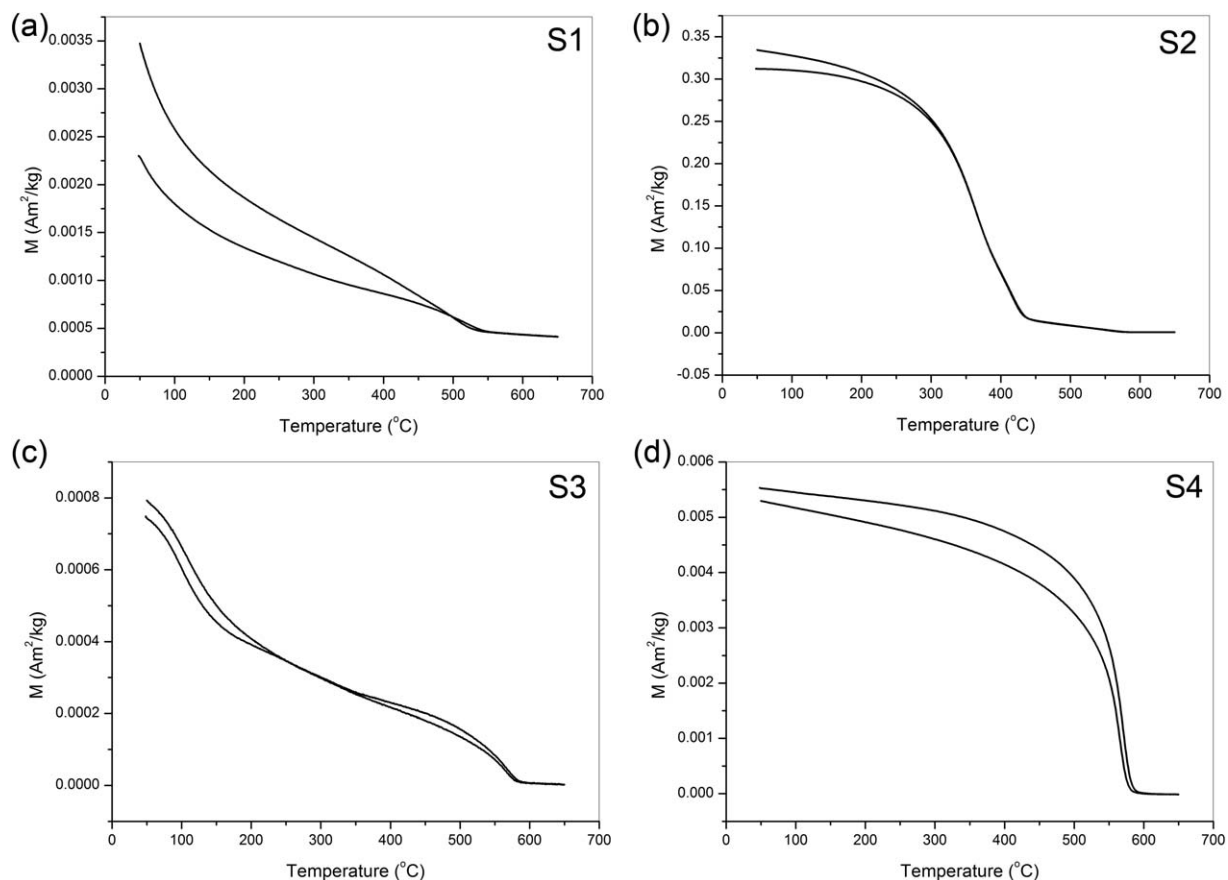
Figure 11. Thermomagnetic curves of samples (a) S1, (b) S2, (c) S3, and (d) S4. Heating was performed in flowing helium, in a field of 100 mT.

samples S1 and S3 display similar thermomagnetic curve behavior (Figure 11) and samples S1 and S2 similar FORC diagrams (Figure 12). The low-temperature Curie values for Samples S1 and S3 are in good agreement with, and hence can be attributed to, grains with the approximate stoichiometry of $Fe_{2.4}Ti_{0.6}O_4$ [*Dunlop and Özdemir*, 1997]. Sample S4 consistently displays the behavior expected for PSD/SD magnetite.

[22] The electron holographic imaging also sheds light on some of the other properties. For example, S1, S2, and S3 were observed to have both a range

of grains sizes and mixed mineralogy as identified from the thermomagnetic analysis. The electron holographic imaging found that the smaller grains were generally far more magnetic than the larger grains. From this we infer that the smaller grains are more Ti-poor titanomagnetite like, as supported by EDX analysis (Figure 5d), and contribute to the near-stoichiometric magnetite Curie temperatures (Table 2), and the larger grains are Ti-rich titanomagnetites giving rise to the low Curie-temperature phase, i.e., the titaniam preferentially resides in the larger titanomagnetite crystals. The flip side of this statement is that the smaller SD-like better magnetic recorders are more likely to be small SD-like magnetite crystals. The problem remains that commonly the magnetic mineralogy of a sample is determined by measuring the Curie temperature in a relatively large magnetic field: this maybe misleading as the magnetic remanence carriers are not necessarily the biggest contributers to high-field thermomagnetic curves.

Table 2. Hysteresis Parameters and Curie Temperatures

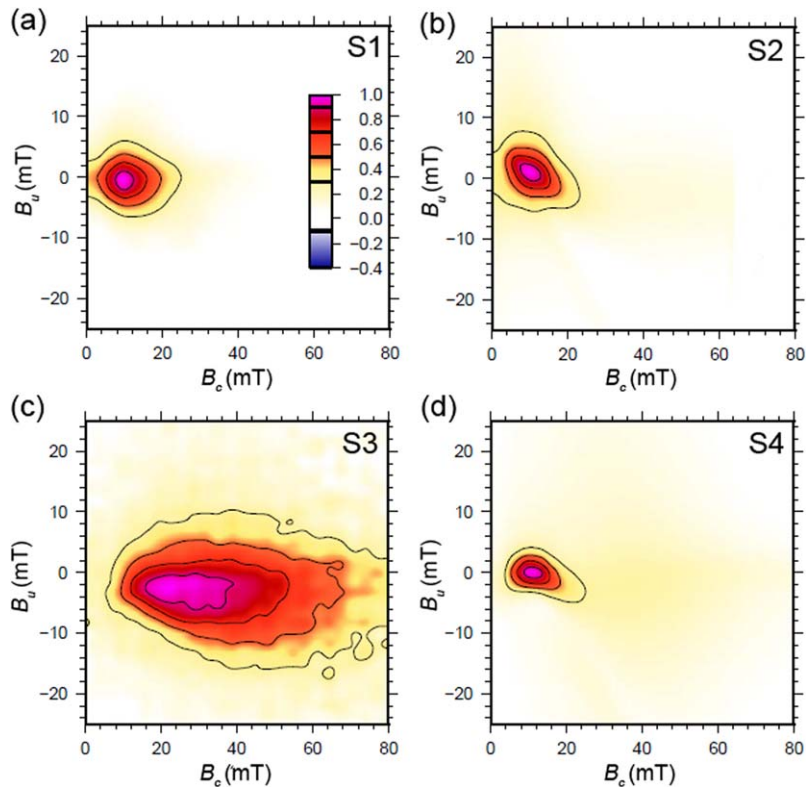| Sample	B_c (mT)	B_{cr} (mT)	M_{rs}/M_s	T_c (°C)
S1	14	18	0.45	83 and 569
S2	19	40	0.33	382–432 and 579
S3	28	55	0.39	119 and 579
S4	27	58	0.24	579

Figure 12. FORC diagrams for samples: (a) S1, (b) S2, (c) S3, and (d) S4. The smoothing factor (SF) for each of the diagrams was two. The measurement time was 250 ms.
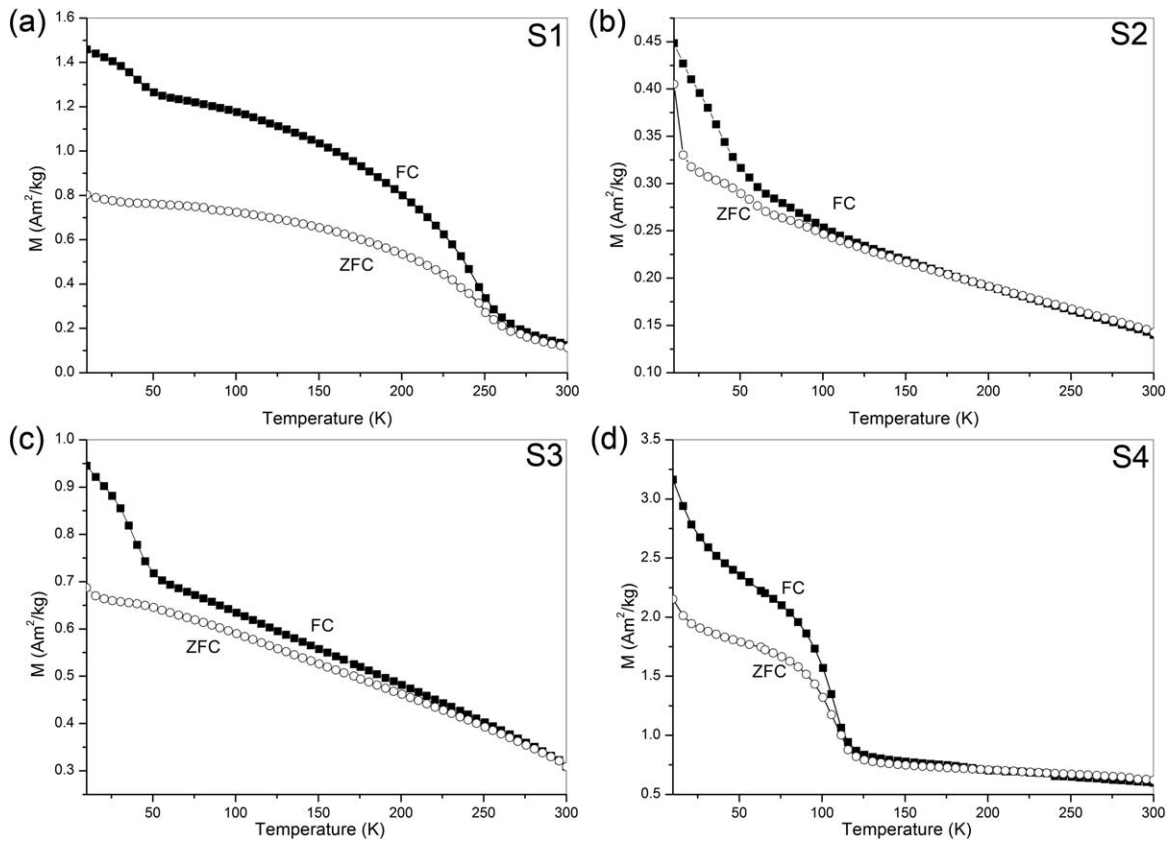

Figure 13. SIRM warming curves from 10 K to 300 K for samples (a) S1, (b) S2, (c) S3, and (d) S4, after field-cooling (FC) and zero-field cooling (ZFC) from room-temperature. A field of 2.5 T was applied.
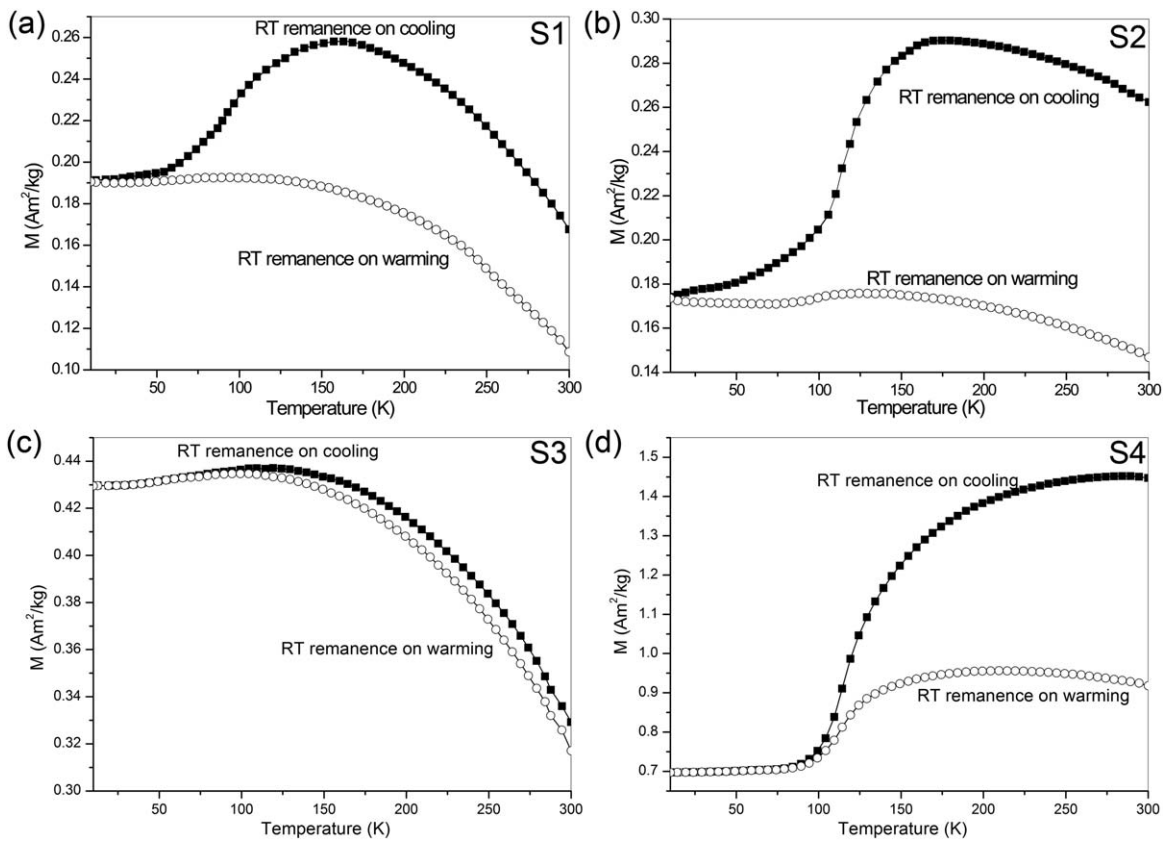
Figure 14. Room-temperature SIRM cycling curves from 300 K to 10 K to 300 K for samples (a) S1, (b) S2, (c) S3, and (d) S4. The SIRM was induced in a field of 2.5 T (check).
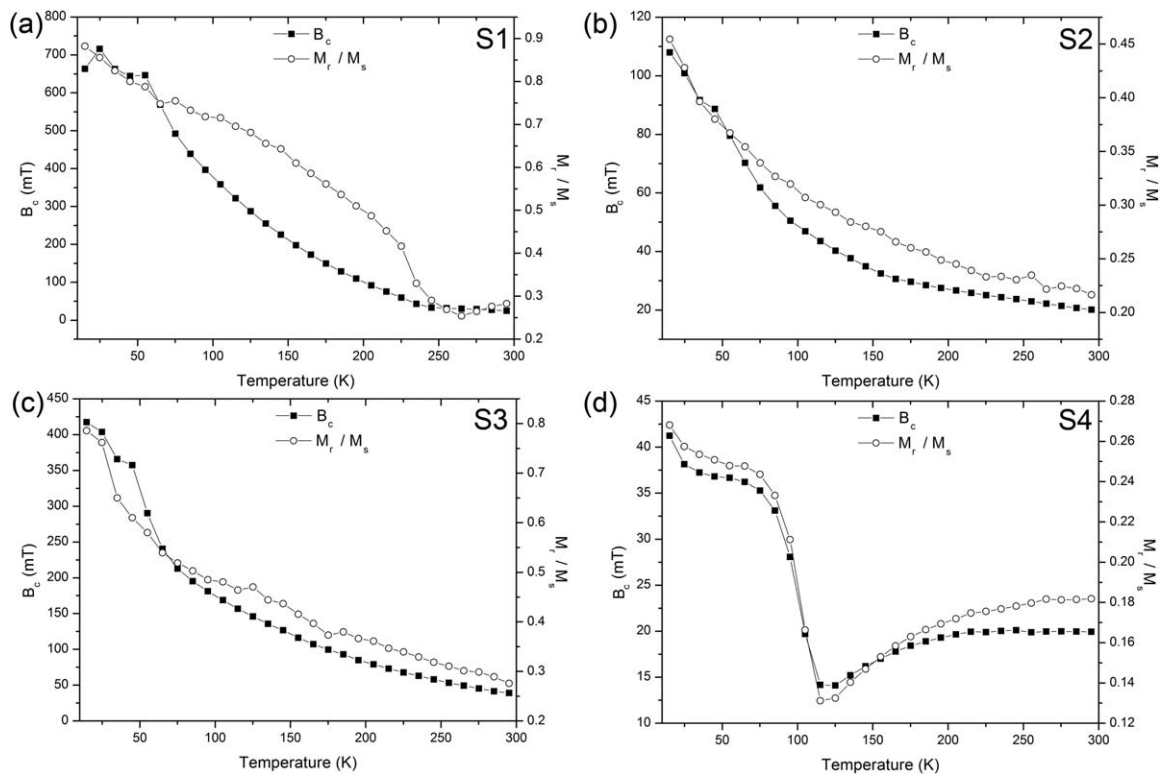

Figure 15. Coercive force and M_{rs}/M_s versus temperature for: (a) S1, (b) S2, (c) S3, and (d) S4.

[23] We believe these samples are ideal in terms of characterization and understanding, for studying natural systems under controlled conditons.

5. Conclusions

[24] Synthetic basalts considered similar to pillow basalts found at mid-ocean ridges have been successfully produced by a glass-ceramic method. The reaction products are composed mainly of $Fe_{3-x}Ti_xO_4$, pyroxene hedenbergite, fayalite, and SiO_2. Magnetic measurements show their bulk characteristics fall into two groups: Ti-rich titanomagnetite samples with varying Ti content; and near-stoichiometric magnetite. In the Ti-rich titanomagnetite samples, off-axis electron holography showed the small $Fe_{3-x}Ti_xO_4$ grains (<50 nm) confined within glassy pyroxene regions to be Fe-rich and single domain, carrying strong magnetic signals, as compared to magnetically weak larger $Fe_{3-x}Ti_xO_4$ grains ($x \sim 0.6$). In contrast, the large grains in the pure magnetite sample are shown by off-axis holography to be pseudo-single domain in nature. These reaction products are thought to be ideal in terms of characterization and understanding, for the purpose of studying natural systems.

Acknowledgments

References

Beggan, C., and C. W. Hamilton (2010), New image processing software for analyzing object size-frequency distributions, geometry, orientation, and spatial distribution, *Computers & Geosciences*, 36, 539–549.

Bleil, U., and N. Petersen (1983), Variation in magnetization intensity and low-temperature titanomagnetite oxidation of ocean floor basalts, *Nature*, 301, 384–388.

Dantzig, J. A., and M. Rappaz (2009), *Solidification*, 287 pp., EFPL Press, Switzerland.

Dunin-Borkowski, R. E., M. R. McCartney, R. B. Frankel, D. A. Bazylinski, M. Pósfai, and P. R. Buseck (1998), Magnetic microstructure of magnetotactic bacteria by electron holography, *Science*, 282, 1868–1870, doi:10.1126/science.282.5395.1868.

Dunlop, D. J., and Ö. Özdemir (1997), *Rock magnetism: Fundamentals and frontiers*, 573 pp., Cambridge Univ. Press, Cambridge, U. K.

Halgedahl, S. L. (1991), Magnetic domain patterns observed on synthetic Ti-rich titanomagnetite as a function of temperature and in states of thermoremanent magnetization, *J. Geophys. Res.*, 96, 3943–3972.

Harrison, R. J., R. E. Dunin-Borkowski, and A. Putnis (2002), Direct imaging of nanoscale magnetic interactions in minerals, *Proc. Natl. Acad. Sci. U. S. A.*, 99, 16,556–16,561.

Hodych, J. P., and J. Matzka (2004), Saturation magnetostriction and its low-temperature variation inferred for natural titanomaghemites: Implications for internal stress control of coercivity in oceanic basalts, *Geophys. J. Int.*, 157, 1017–1026, doi:10.1111/j.1365-246X.2004.02231.x.

Kasama, T., R. E. Dunin-Borkowski, and M. Beleggia (2011), *Electron holography of magnetic materials, in* Holography—Different Fields of Application, edited by F. A. Monroy Ramírez, pp. 53–80, InTech, Croatia.

Kasama, T., R. J. Harrison, N. S. Church, M. Nagao, J. M. Feinberg, and R. E. Dunin-Borkowski (2013), Ferrimagnetic/ferroelastic domain interactions in magnetite below the Verwey transition. Part I: Electron holography and Lorentz microscopy, *Phase Trans.*, 86, 67–87.

Krása, D., V. P. Shcherbakov, T. Kunzmann, and N. Petersen (2005), Self-reversal of remanent magnetization in basalts due to partially oxidized titanomagnetites, *Geophys. J. Int.*, 162, 115–136.

Moskowitz, B. M., S. L. Halgedahl, and C. A. Lawson (1988), Magnetic domains on unpolished and polished surfaces of titanium-rich titanomagnetite, *J. Geophys. Res.*, 93, 3372–3386.

Moskowitz, B. M., M. J. Jackson, and C. Kissel (1998), Low-temperature magnetic behavior of titanomagnetites, *Earth Planet. Sci Lett.*, 157, 141–149.

Muxworthy, A. R. (1999), Low-temperature susceptibility and hysteresis of magnetite, *Earth Planet. Sci Lett.*, 169, 51–58.

Muxworthy, A. R., and E. McClelland (2000), The causes of low-temperature demagnetization of remanence in multidomain magnetite, *Geophys. J. Int.*, 140, 115–131.

Muxworthy, A. R., and D. J. Dunlop (2002), First-order reversal curve (FORC) diagrams for pseudo-single-domain magnetites at high temperature, *Earth Planet. Sci Lett.*, 203, 369–382.

Muxworthy, A. R., D. Heslop, and W. Williams (2004), Influence of magnetostatic interactions on first-order-reversal-curve (FORC) diagrams: A micromagnetic approach, *Geophys. J. Int.*, 158, 888–897.

Newell, A. J. (2005), A high-precision model of first-order reversal curve (FORC) functions for single-domain ferromagnets with uniaxial anisotropy, *Geochem. Geophys. Geosyst.*, 6, Q05010, doi:10.1029/2004GC000877.

Özdemir, Ö., and S. K. Banerjee (1981), An experimental study of magnetic viscosity in synthetic monodomain titanomagnetite: Implications for the magnetization of the ocean crust, *J. Geophys. Res.*, 86, 11,864–811,868.

Özdemir, Ö., and D. J. Dunlop (2003), Low-temperature behavior and memory of iron-rich titanomagnetites (Mt. Haruna, Japan and Mt. Pinatubo, Philippines), *Earth Planet. Sci. Lett.*, 216, 193–200.

Pike, C. R., A. P. Roberts, and K. L. Verosub (1999), Characterizing interactions in fine magnetic particle systems using first order reversal curves, *J. Appl. Phys.*, 85, 6660–6667.

Roberts, A. P., C. R. Pike, and K. L. Verosub (2000), First-order reversal curve diagrams: A new tool for characterizing the magnetic properties of natural samples, *J. Geophys. Res.*, 105, 28,461–28,475.

Shaar, R., and J. M. Feinberg (2013), Rock magnetic properties of dendrites: Insights from MFM imaging and implications for paleomagnetic studies, *Geochem. Geophys. Geosyst.*, *14*, 407–421, doi:10.1002/ggge.20053.

Tarduno, J., and R. Cottrell (2005), Dipole strength and variation of the time-averaged reversing and nonreversing geodynamo based on Thellier analyses of single plagioclase crystals, *J. Geophys. Res.*, *110*, B11101, doi:10.1029/2005JB003970.

Tauxe, L (2002), *Paleomagnetic Principles and Practice*, 299 pp., Kluwer Academic Publishers, Netherlands.

Worm, H.-U., and H. Markert (1987), The preparation of dispersed titanomagnetite particles by the glass-ceramic method, *Phys. Earth Planet. Inter.*, *46*, 263–270.

Zhou, W. M., R. Van der Voo, and D. R. Peacor (1997), Single-domain and superparamagnetic titanomagnetite with variable Ti content in young ocean-floor basalts: No evidence for rapid alteration, *Earth Planet. Sci. Lett.*, *150*, 353–362, doi:10.1016/s0012-821x(97)00099-x.

Zhou, W. M., R. Van der Voo, D. R. Peacor, and Y. X. Zhang (2000), Variable Ti-content and grain size of titanomagnetite as a function of cooling rate in very young MORB, *Earth Planet. Sci. Lett.*, *179*, 9–20.

Zitzelsberger, A., and E. Schmidbauer (1996), Magnetic properties of synthetic milled an annealed titanomagnetite ($Fe_{2.3}Ti_{0.7}O_4$) particles 1–125 μm in diameter and analysis of their microcrystalline structure, *Geophys. Res. Lett.*, *23*, 2855–2858.